

Supplementary Information

Photocatalytic oxygen-atom transmutation of oxetanes

Ying-Qi Zhang¹, Shuo-Han Li¹, Xinglong Zhang^{2*} & Ming Joo Koh^{1*}

¹Department of Chemistry, National University of Singapore, 4 Science Drive 2, Republic of Singapore, 117544.

²Department of Chemistry, The Chinese University of Hong Kong, Shatin, New Territories, Hong Kong, China.

*Corresponding authors: chmkmj@nus.edu.sg, xinglong.zhang@cuhk.edu.hk

Table of contents

1. General.....	3
Solvents.....	4
Substrates	4
2. Supplementary Tables.....	29
Supplementary Table 1. Evaluation of reaction conditions.	29
Supplementary Table 2. Evaluation of reaction parameters.	30
Supplementary Table 3. Unsuccessful studies using Vilsmeier-Haack reagents and Appel reaction conditions.	31
3. Photocatalytic Oxygen-Atom Transmutation	32
Experimental procedures	32
4. Late-Stage Editing and Applications	80
Late-stage editing with densely functionalized bioactive amines.....	80
Late-stage editing of complex bioactive oxetanes	85
O-to-C transmutation to afford 1,1-difluorocyclobutane isostere.....	88
Synthesis of the key precursor of respiratory syncytial virus inhibitor	90
Synthesis of the key precursor of cyclin-dependent kinase 2 inhibitor	93
5. Mechanistic Investigations.....	96
Control experiments to probe dibromide intermediate	96
Control experiments to probe alkyl formate intermediate	97
6. Density Functional Theory (DFT) Calculations	98
Computational methods	98
Model reaction	99
Conformational Considerations	99

Most favourable pathway.....	100
Oxetane reactivity with complex I	101
Chemoselectivity between cyclic and acyclic ethers	102
DFT-optimised structures	104
Molecular origins of chemoselectivity.....	107
Simple transition state theory (TST) for rate estimation	112
Fukui reactivity index calculation.....	113
Optimised structures and absolute energies	113
7. NMR Spectra	116
8. X-ray Crystallographic Data	234
9. References.....	240

6. Density Functional Theory (DFT) Calculations

Computational methods

Kohn-Sham density functional theory (KS-DFT) calculations were performed with *Gaussian 16* rev. B.01.⁸ The global hybrid DFT functional M06-2X⁹ with the def2-SVPD^{10,11} Karlsruhe-family basis set for Br atom and def2-SVP^{10,12} basis set for all other atoms (this mixed basis set is denoted BS1) with implicit SMD continuum solvation model¹³ for N,N-dimethyl formamide (DMF) solvent was used for geometry optimization. The “D” in def2-SVPD basis set denotes diffuse functions which are important for the correct description of anionic electron distributions.¹⁴⁻¹⁶ Minima and transition structures on the potential energy surface (PES) were confirmed as such by harmonic frequency analysis, showing respectively zero and one imaginary frequency. M06-2X was chosen as it has shown good accuracy in the study of organocatalytic systems.¹⁷⁻²⁷ For the SMD(DMF)-M06-2X/BS1 optimized structures, single point (SP) corrections were performed using M06-2X functional and def2-TZVPD^{10,11} basis set for Br atom and def2-TZVP^{10,12} basis set for all other atoms (denoted BS2) in the implicit SMD continuum for DMF solvent to improve upon the accuracy of the calculated energies. All DFT calculations were submitted using our automation toolkit CHEMSMART.²⁸

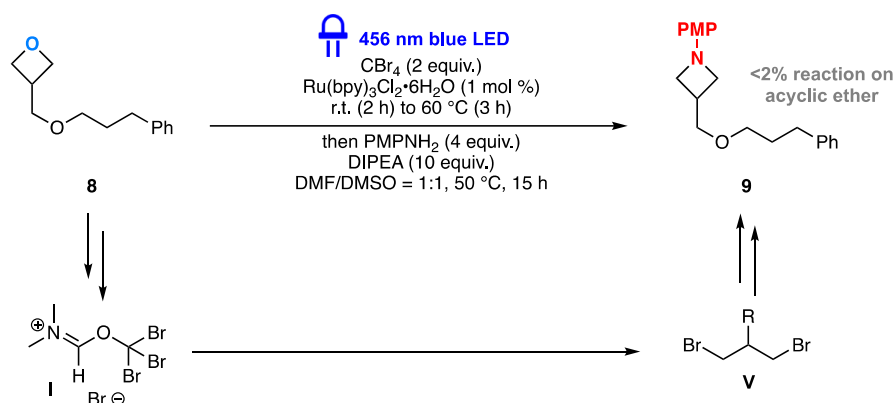
Gibbs energies were evaluated at the room temperature of 25°C, using Grimme’s scheme of quasi-RRHO treatment of vibrational entropies,²⁹ using the CHEMSMART code. Vibrational entropies of frequencies below 100 cm⁻¹ were obtained according to a free rotor description, using a smooth damping function to interpolate between the two limiting descriptions. The free energies reported in Gaussian from gas-phase optimisation were further corrected using standard concentration of 1 mol/L,³⁰⁻³² which were used in solvation calculations, instead of the gas-phase 1atm used by default in Gaussian program. Unless otherwise stated, the final SMD(DMF)-M06-2X/BS2//M06-2X/BS1 Gibbs energies are used for discussion throughout. *All Gibbs energy values in the text and figures are quoted in kcal/mol.*

Non-covalent interactions (NCIs) were analyzed using NCIPLOT³³ calculations. The *.wfn* files for NCIPLOT were generated at M06-2X/BS1 level of theory. NCI indices calculated with NCIPLOT were visualized at a gradient isosurface value of $s = 0.5$ au. These are colored according to the sign of the second eigenvalue (λ_2) of the Laplacian of the density ($\nabla^2\rho$) over the range of -0.1 (blue = attractive) to $+0.1$ (red = repulsive). Molecular orbitals are visualized using an isosurface value of 0.05 au throughout.

All molecular structures and molecular orbitals are visualized using *PyMOL*³⁴ software, which *.pse* files were prepared using our CHEMSMART package.

Model reaction

Supplementary Figure 3 shows the model reaction that we used for computational studies of the reaction mechanism for the conversion of species **I** to species **V**.



Supplementary Figure 3. Model reaction used in computational modelling.

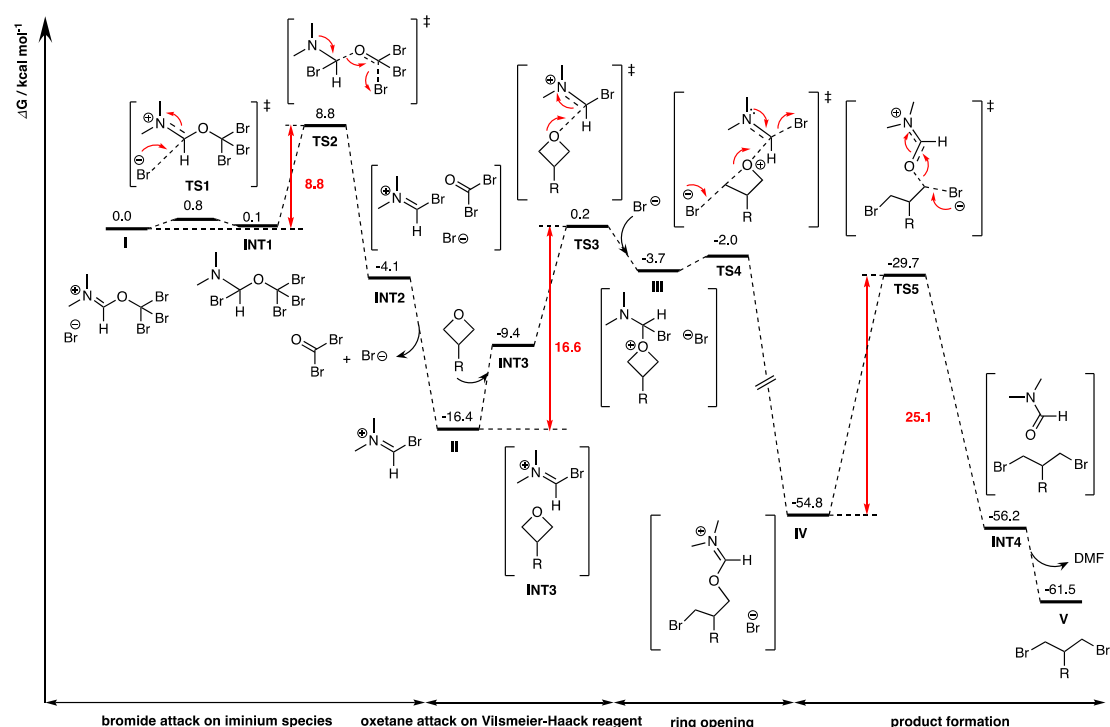
Conformational Considerations

Conformational sampling was performed for the cationic iminium species of complex **I** using Grimme's *CREST* program,^{35,36} which used metadynamics (MTD) with genetic z-matrix crossing (GC) performed at the GFN2-xTB³⁷⁻³⁹ extended semiempirical tight-binding level of theory with *opt=vtight* option. Two distinct conformers were located after further DFT optimization. The lowest energy structure is used for all subsequent studies.

Most favourable pathway

The most favourable reaction pathway occurs when the iminium species in complex **I** is attacked by bromide anion, via **TS1**, with a very small barrier of 0.8 kcal/mol, to give an almost isoenergetic species **INT1** (Supplementary Figure 4). This step is reversible, giving complex **I** and **INT1** in equilibrium. Next, **INT1** can undergo a C–O bond cleavage via **TS2**, with a barrier of 8.8 kcal/mol from **I**, to give the Vilsmeier-Haack reagent (**II**), carbonyl bromide (Br_2CO) and bromide anion as complex **INT2**. The release of Br_2CO and Br^- gives **II** which is highly exergonic, being downhill of starting complex **I** by -16.4 kcal/mol. Thus, the formation of give Vilsmeier-Haack reagent **II** is highly thermodynamically favourable.

The subsequent addition of oxetane substrate gives complex **INT3** that is 7.0 kcal/mol uphill of **II**. The attack of the imine group by the oxetane oxygen atom occurs via **TS3**, with a barrier of 16.6 kcal/mol from the Vilsmeier-Haack reagent **II**. Next, bromide anion attacks the carbon atom on the oxetane ring, via **TS4**, with a small barrier of 1.7 kcal/mol from complex **III**, to give ring-opened species **IV**. This step is highly exergonic and thermodynamically favourable, as the ring-opened species **IV** lies 51.1 kcal/mol downhill of complex **III**. Thus, from the Vilsmeier-Haack reagent **II**, once the oxetane attacks the iminium to form complex **III**, the subsequent ring opening is facile and both kinetically and thermodynamically favourable, giving ring-opened intermediate **IV**. This step has an overall barrier of 16.6 kcal/mol (from **II** to **TS3**) and is thermodynamically downhill by 38.4 kcal/mol (from **II** to **IV**).



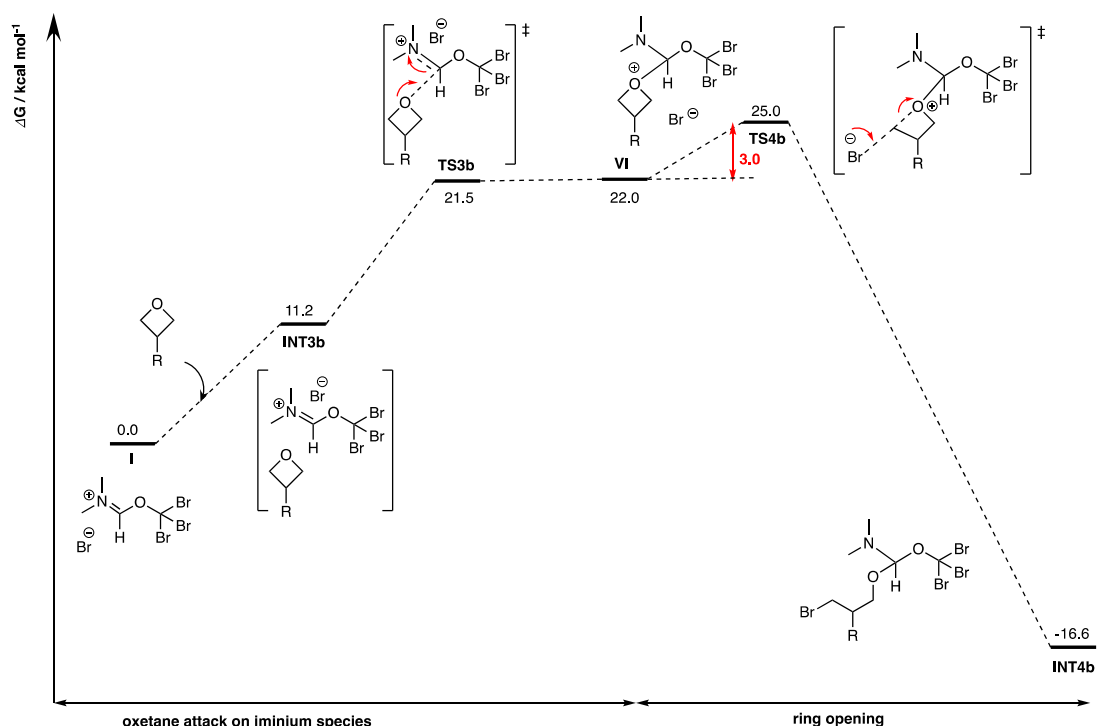
Supplementary Figure 4. Gibbs energy profile for the conversion of complex **I to complex **V**.**

Next, the bromide anion attacks the C–O bond through S_N2 mechanism via **TS5**, with an overall barrier of 25.1 kcal/mol from species **IV**, to give an almost isoenergetic but slightly downhill dibromide complexed with DMF molecule, **INT4**. The release of DMF molecule from this complex is exergonic and gives the dibromide, **V**, at -61.5 kcal/mol, which is 6.7 kcal/mol downhill of **IV**. Overall, the formation of **V** from **I** is thermodynamically favourable, with Gibbs energy of reaction, $\Delta G_r = -61.5$ kcal/mol. The rate-limiting step is the formation of second C–Br bond via **TS5**, with a barrier of 25.1 kcal/mol.

Oxetane reactivity with complex **I**

For complex **I**, we also considered the possibility that the oxetane oxygen directly attacks the imine group of the iminium species. The Gibbs energy profile is shown in Supplementary Figure 5. The formation of **I** with oxetane gives complex **INT3b**, which is uphill by 11.2 kcal/mol. Subsequently, the oxetane oxygen can attack the imine group, via **TS3b**, which has a barrier of 21.5 kcal/mol from species **I**, to give a rather unstable species **VI**. This species can undergo ring opening via **TS4b**, with a barrier of 3.0

kcal/mol from **VI** (overall barrier of 25.0 kcal/mol from complex **I**), to given complex **INT4b**, which is downhill of complex **I**, by -16.6 kcal/mol.



Supplementary Figure 5. Gibbs energy profile for the attack of complex **I to by oxetane.**

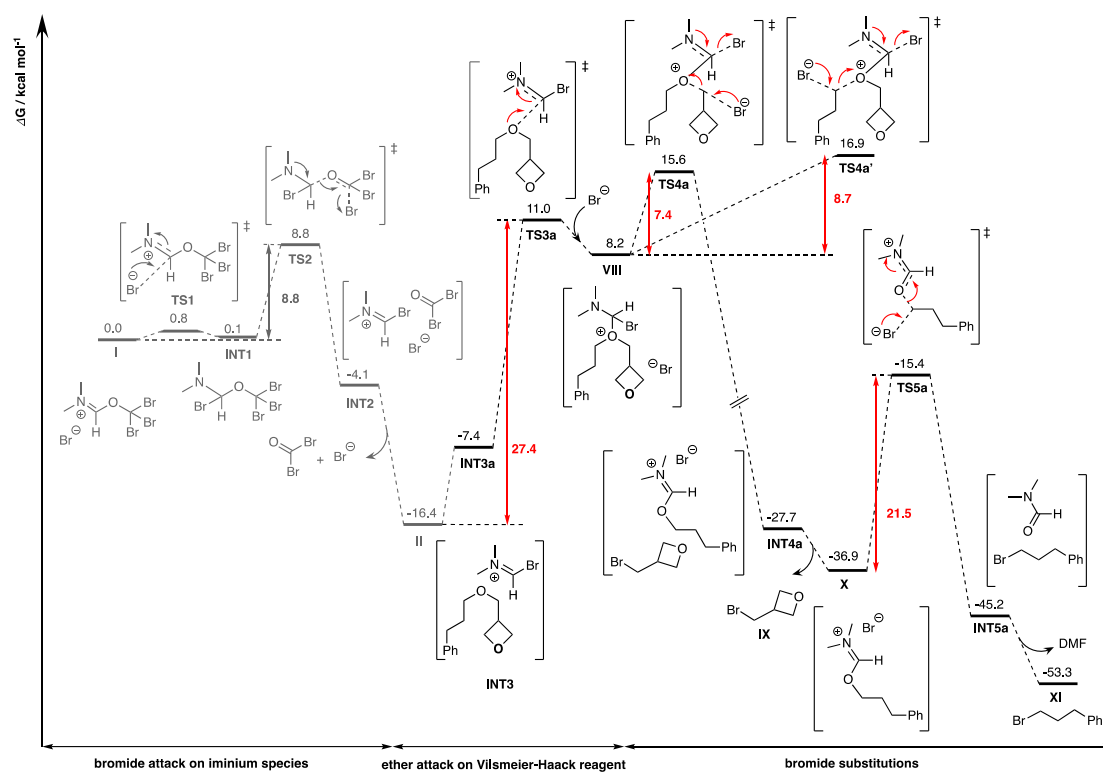
Although the formation of complex **INT4b** from **I** is thermodynamically favourable and kinetically feasible, however, complex **I** will be preferentially attacked by bromide ion, via **TS2** with a barrier of 8.8 kcal/mol (Supplementary Figure 4), instead of attacked by oxetane oxygen, via **TS3b**, with a higher barrier of 21.5 kcal/mol (Supplementary Figure 5). Thus, the formation of the Vilsmeier-Haack reagent **II** is kinetically favoured over the reaction of oxetane oxygen with complex **I**, by 12.7 kcal/mol (rate ratio of about 2 billion : 1 using simple transition state theory as an estimate at room temperature, Section **Simple transition state theory (TST) for rate estimation**).

Chemoselectivity between cyclic and acyclic ethers

After the full mechanism for the conversion of species **I** to species **V** is elucidated (Supplementary Figure 4), we focus on the steps for the oxygen attack on the iminium

group of the Vilsmeier-Haack reagent **II** (**TS3**) and the subsequent bromide attack (**TS4**) to understand the chemoselectivity outcomes (comparing attack by oxetane oxygen vs acyclic ether oxygen). After the formation of the Vilsmeier-Haack reagent **II**, it can form complex with substrate to give **INT3a** (conformer of **INT3**, Supplementary Figure 4) where the ether oxygen is close to the iminium carbon. This complex is 9.0 kcal/mol uphill of **II**. The subsequent attack of iminium group by ether oxygen occurs via **TS3a**, with a barrier of 27.4 kcal/mol from **II**, to give complex **VIII**, which is uphill of **INT3a** by 15.6 kcal/mol. The bromide anion can then attack **VIII** at two different carbon positions, via **TS4a** or **TS4a'**. From **VIII**, attack on the carbon adjacent to the oxetane group, via **TS4a**, gives a barrier of 7.4 kcal/mol, but attack on the other carbon, via **TS4a'**, gives a higher barrier of 8.7 kcal/mol.

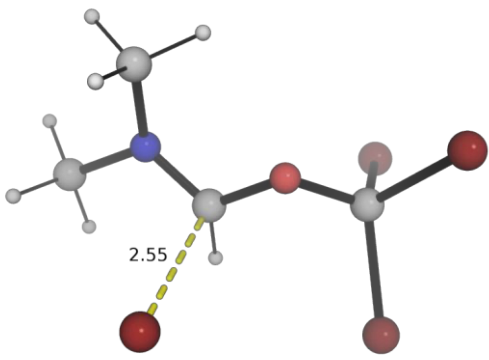
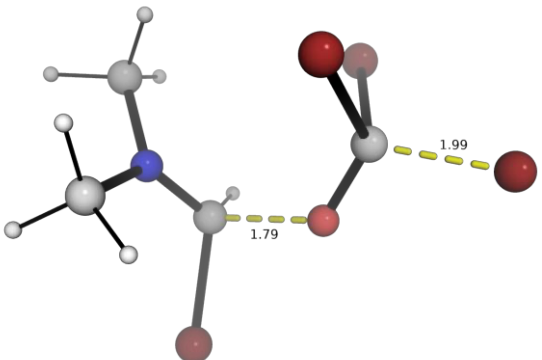
We observe that for the major pathway shown in Supplementary Figure 4, the attack on iminium carbon by oxetane oxygen (**TS3**) has a higher barrier than the subsequent ring opening by bromide anion (**TS4**). On the other hand, in Supplementary Figure 6 for the competing pathway, the attack on iminium carbon by ether oxygen (**TS3a**) has a lower barrier than the subsequent C–Br bond formation by bromide anion (**TS4a**). This is likely attributed to the fact that the release of ring strain makes the ring opening (**TS4**) for C–Br bond formation more facile than the C–Br bond formation in **TS4a** which does not benefit from release of ring strain.

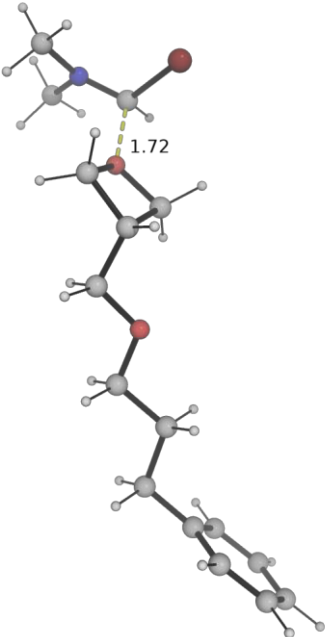
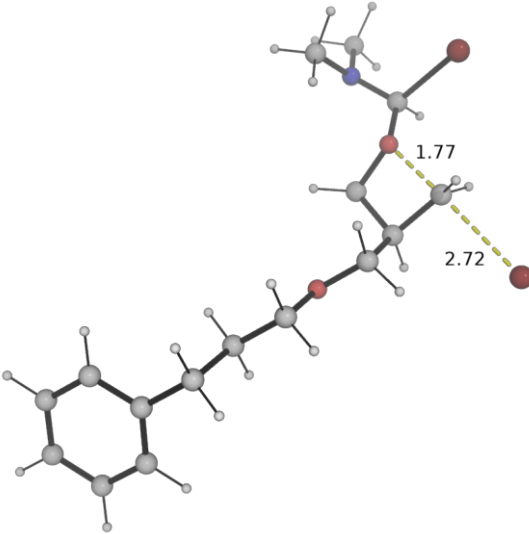
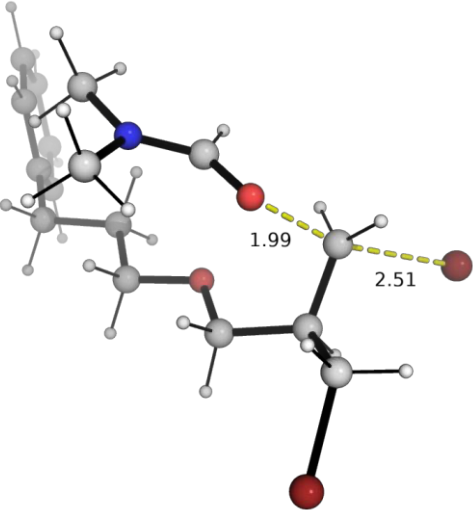
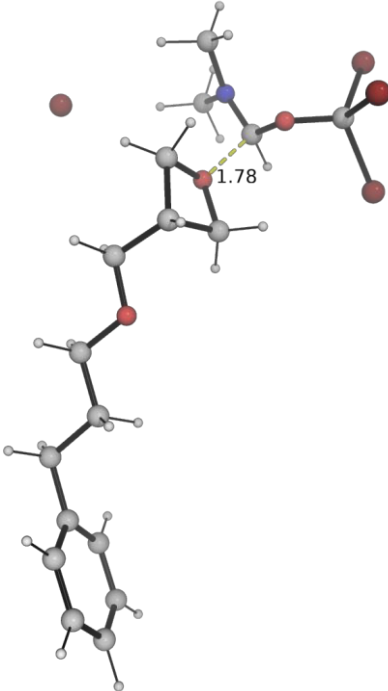


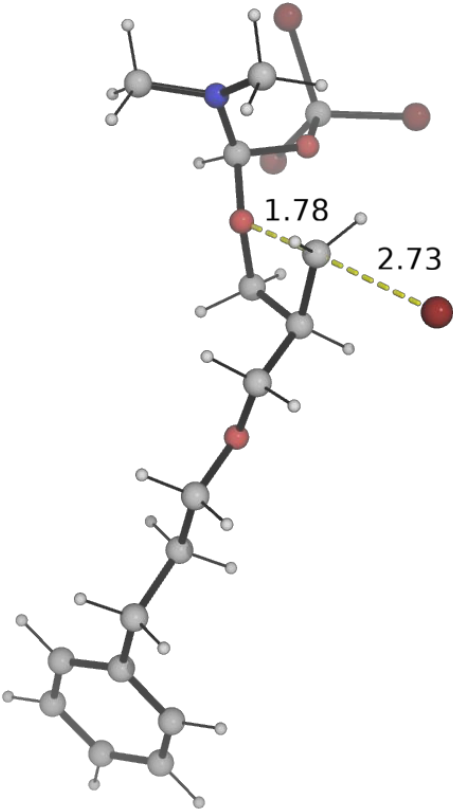
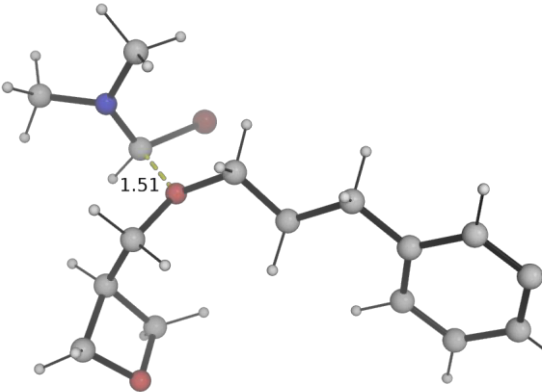
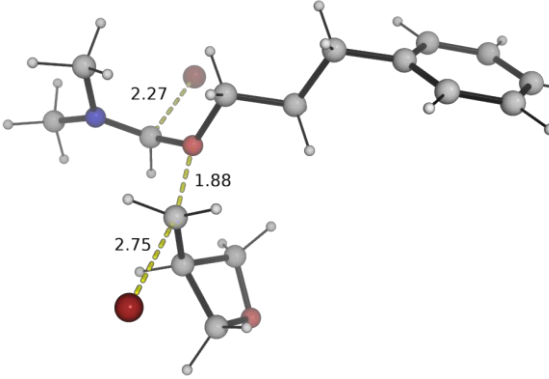
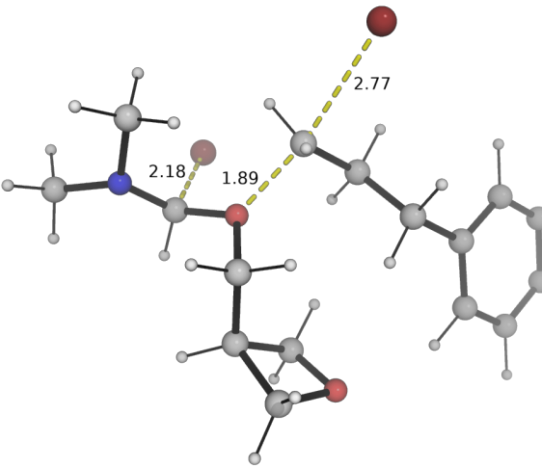
Supplementary Figure 6. Gibbs energy profile for chemoselectivity studies.

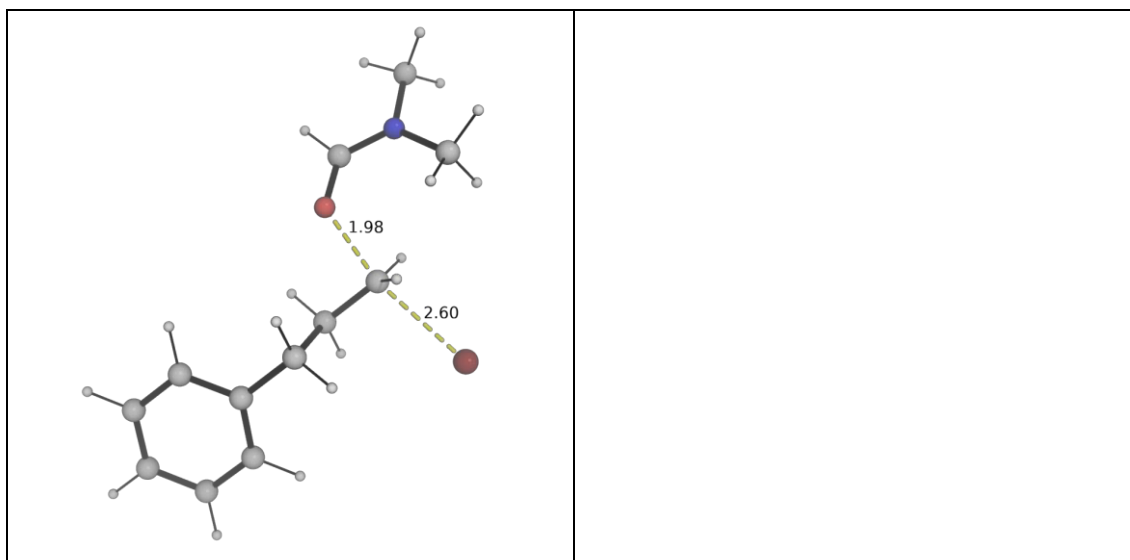
DFT-optimised structures

Selected DFT-optimised structures are shown in Supplementary Figure 7.

TS1	TS2
$\Delta G^\ddagger = 0.8$	$\Delta G^\ddagger = 8.8$
	
TS3	TS4
$\Delta G^\ddagger = 0.2$	$\Delta G^\ddagger = -2.0$

	
<p>TS5</p>	<p>TS3b</p>
<p>$\Delta G^\ddagger = -29.7$</p>	<p>$\Delta G^\ddagger = 21.5$</p>
	
<p>TS4b</p>	<p>TS3a</p>
<p>$\Delta G^\ddagger = 25.0$</p>	<p>$\Delta G^\ddagger = 11.0$</p>

	
<p>TS4a</p>	<p>TS4a'</p>
<p>$\Delta G^\ddagger = 15.6$</p>	<p>$\Delta G^\ddagger = 16.9$</p>
	
<p>TS5a</p>	
<p>$\Delta G^\ddagger = -15.4$</p>	



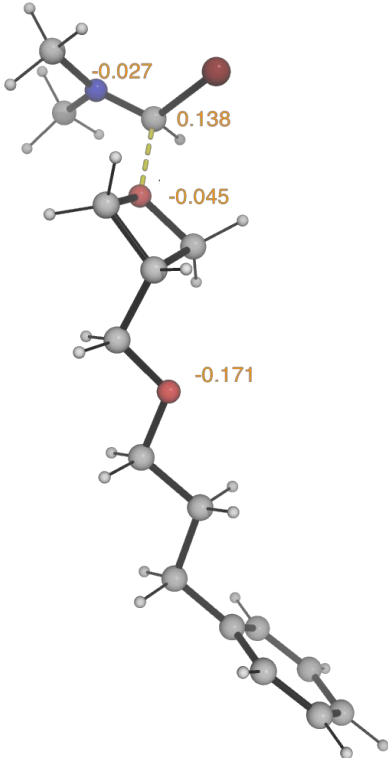
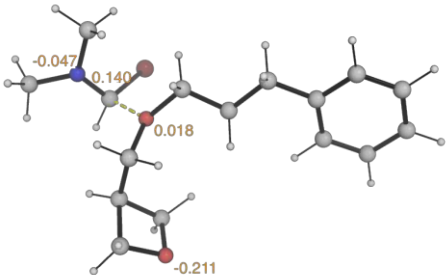
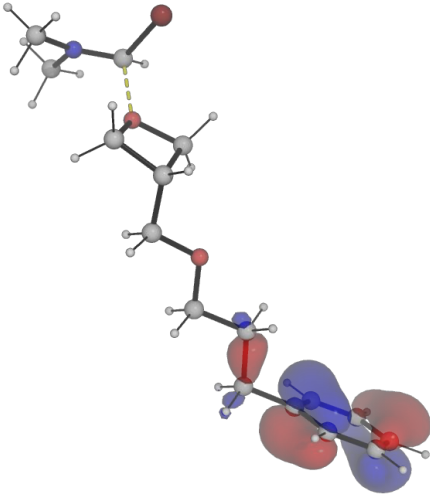
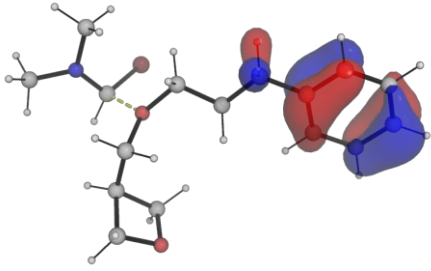
Supplementary Figure 7. DFT-optimized structures for the transition states.

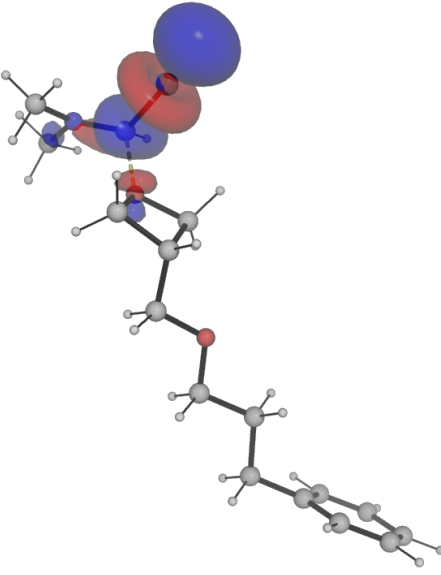
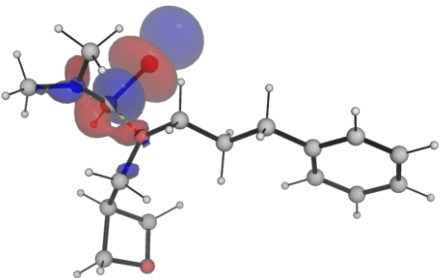
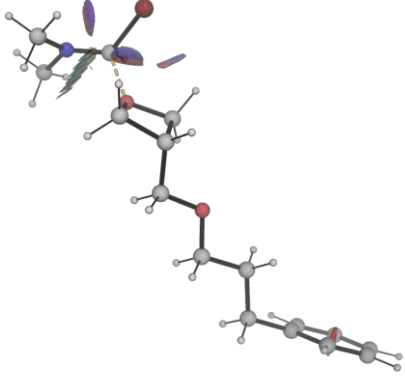
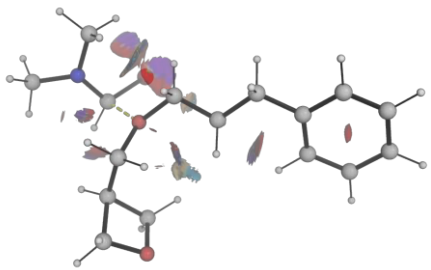
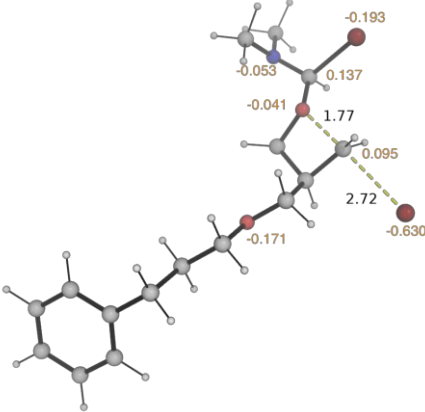
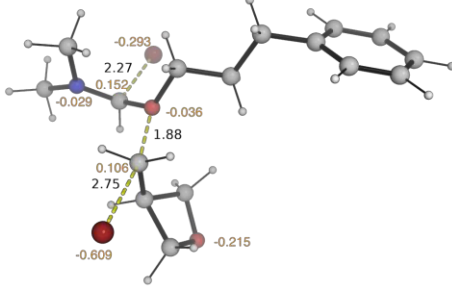
Molecular origins of chemoselectivity

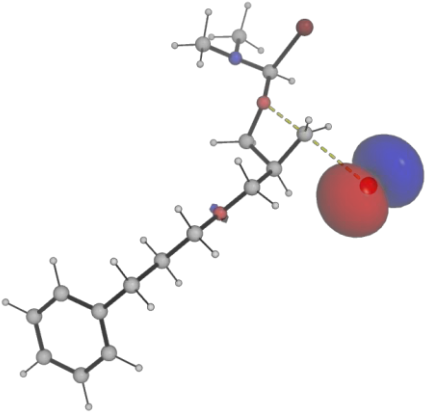
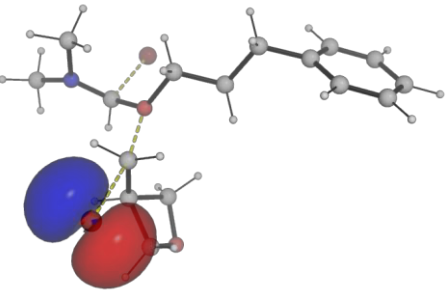
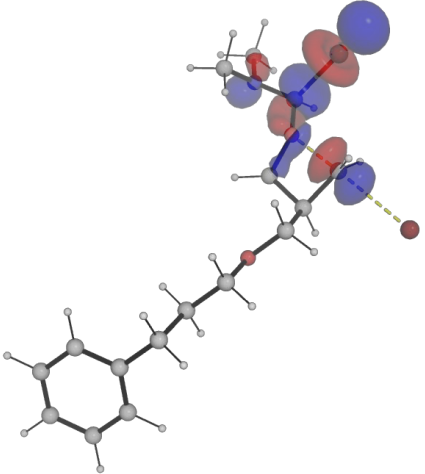
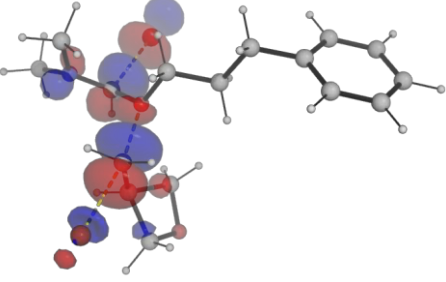
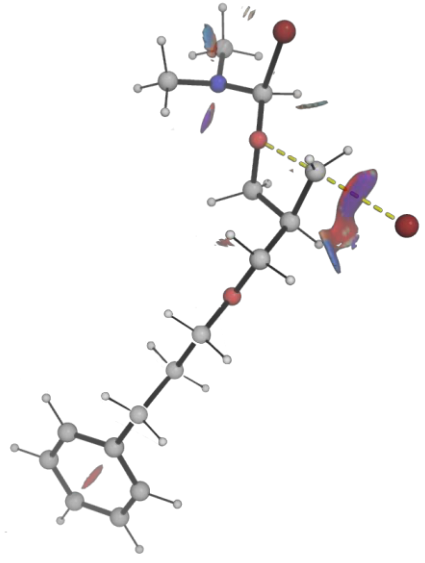
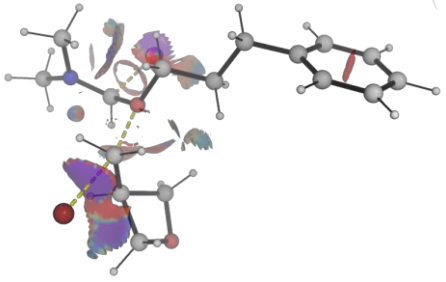
Comparing the barriers of **TS3** and **TS3a**, we see that **TS3** has a lower barrier by 10.8 kcal/mol than **TS3a**. This translates to a kinetic preference for **TS3** over **TS3a** by a factor of 30 million : 1, using simple transition state theory. In other words, attack on the iminium carbon of the Vilsmeier-Haack reagent **II** by the oxetane oxygen is much more favourable than that by the ether oxygen.

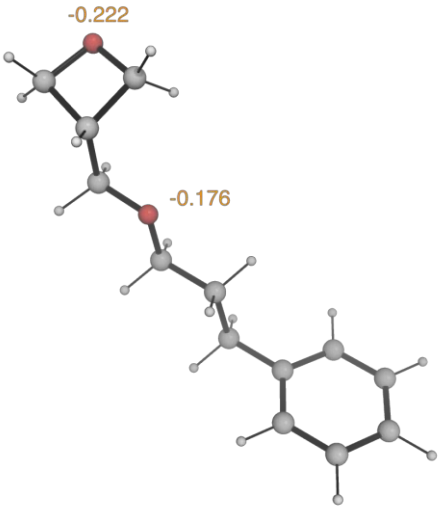
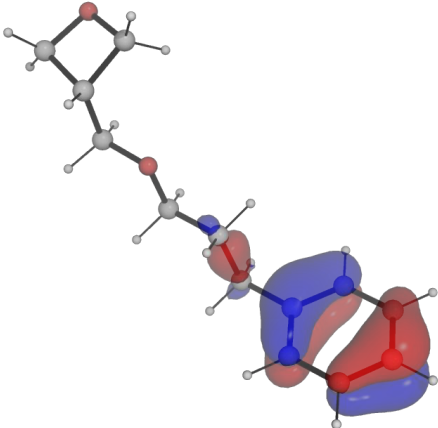
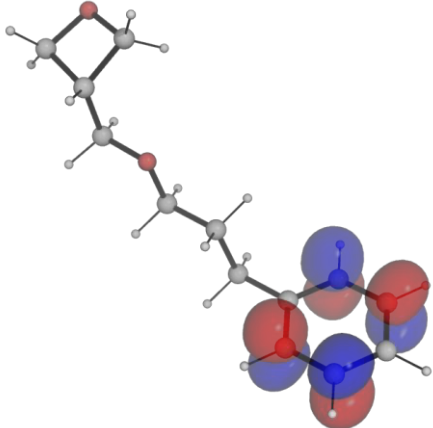
Analysis of Hirshfeld charges⁴⁰ (charge scheme less dependent on DFT basis sets) on substrate **8** indicates that the oxetane oxygen atom has a more negative charge at -0.222 a.u., which is more negative than the charge at ether oxygen, at -0.176 a.u., by 0.046 a.u., suggesting that the oxetane oxygen is more nucleophilic than the ether oxygen. The Fukui reactivity index (f^-) also shows that the oxetane oxygen is much more nucleophilic than the ether oxygen (Section **Fukui reactivity index calculation**).

In addition, the Hirshfeld charges of key atoms in **TS3** and **TS3a** shows that the ether oxygen atom becomes slightly positive in the **TS3a** (0.018 a.u., Supplementary Figure 8) as it attacks the iminium carbon of the Vilsmeier-Haack reagent **II**, making the transition state less favourable as a positive charge develops on oxygen atom. On the other hand, the oxetane oxygen in **TS3** has a negative charge of -0.045 a.u. (Supplementary Figure 8). HOMO and LUMO diagrams and non-covalent interactions (NCI) plots for **TS3** and **TS3a** are similar (Supplementary Figure 8).

	TS3	TS3a
Hirshfeld charges	 <p>Diagram of the transition state TS3 showing Hirshfeld charges. The charges are: -0.027 (on the nitrogen atom), 0.138 (on the carbon atom bonded to nitrogen), -0.045 (on the oxygen atom), and -0.171 (on the carbon atom bonded to the oxygen atom). The structure is a ball-and-stick model with dashed lines indicating the transition state geometry.</p>	 <p>Diagram of the transition state TS3a showing Hirshfeld charges. The charges are: -0.047 (on the nitrogen atom), 0.140 (on the carbon atom bonded to nitrogen), 0.018 (on the oxygen atom), and -0.211 (on the carbon atom bonded to the oxygen atom). The structure is a ball-and-stick model with dashed lines indicating the transition state geometry.</p>
HOMO	 <p>Diagram of the transition state TS3 showing the Highest Occupied Molecular Orbital (HOMO). The orbital is represented by red and blue lobes, indicating the phase of the wavefunction. The structure is a ball-and-stick model with dashed lines indicating the transition state geometry.</p>	 <p>Diagram of the transition state TS3a showing the Highest Occupied Molecular Orbital (HOMO). The orbital is represented by red and blue lobes, indicating the phase of the wavefunction. The structure is a ball-and-stick model with dashed lines indicating the transition state geometry.</p>

LUMO		
NCI		
	TS4	TS4a
Hirshfeld charges		

HOMO	 <p>Visualization of the Highest Occupied Molecular Orbital (HOMO) for substrate 8. The molecule is shown in a ball-and-stick model with a benzene ring on the left and a side chain on the right. The HOMO is represented by large red and blue lobes, primarily localized on the side chain, indicating the electron-donating character of this region.</p>	 <p>Visualization of the HOMO for the product of the reaction of substrate 8. The orbital distribution is similar to the substrate but shows changes in the side chain, reflecting the chemical transformation.</p>
LUMO	 <p>Visualization of the Lowest Unoccupied Molecular Orbital (LUMO) for substrate 8. The orbital is distributed across the molecule, with significant lobes on the side chain and the benzene ring, representing the electron-accepting character.</p>	 <p>Visualization of the LUMO for the product. The orbital distribution shows a shift in the electron-accepting regions compared to the substrate, particularly in the side chain area.</p>
NCI	 <p>Visualization of the Non-Covalent Interaction (NCI) for substrate 8. The image shows various colored lobes (red, blue, green) representing different types of non-covalent interactions, such as hydrogen bonding and van der Waals forces, within the molecule.</p>	 <p>Visualization of the NCI for the product. The distribution of non-covalent interaction lobes is altered due to the chemical reaction, showing new interaction patterns.</p>
	8 (substrate)	

<p>Hirshfeld charges</p>		
<p>HOMO</p>		
<p>LUMO</p>		

Supplementary Figure 8. Hirshfeld charges, frontier molecular orbitals and non-covalent interactions (NCI) plots for selected species.

Comparing the TSs for the C–Br bond formation steps (**TS4** and **TS4a**, Supplementary Figure 8), the frontier molecular orbitals (FMOs) are also similar, and NCI plots seem to suggest that the NCIs in **TS4a** may be more favourable. Despite these, reaction via

TS4 has a much lower barrier (1.7 kcal/mol from the complex preceding the TS) than that via **TS4a** (7.4 kcal/mol from the complex preceding the TS), likely because the release of oxetane ring strain in **TS4** contributes to lowering the barrier. To summarize, the steps for reaction with the Vilsmeier-Haack reagent **II** and subsequent C–Br bond formation are both energetically more favourable for the oxetane oxygen compared to the ether oxygen, as a consequence of the greater nucleophilicity of the oxetane oxygen and release of ring strain during C–Br formation.

Simple transition state theory (TST) for rate estimation

The barrier difference $\Delta\Delta G^\ddagger$ between two transition states can be used to predict the kinetic preference for the major pathway over the minor pathway, using simple transition state theory as an estimate and without Boltzmann weighting of all the conformers.

The Eyring equation

$$k = \frac{k_B T}{h} e^{-\Delta G^\ddagger / RT}$$

gives the rate constant under simple transition state theory (TST) assumptions.

Under kinetic control, as we compare the barrier heights difference between competing transition states, the ratio of the rates between two pathways is given by:

$$\frac{k_A}{k_B} = \frac{e^{-\Delta G_A^\ddagger / RT}}{e^{-\Delta G_B^\ddagger / RT}} = e^{-\Delta\Delta G^\ddagger / RT}$$

where k_X is the rate constant of pathway X (X=A or B); ΔG_X^\ddagger is the activation barrier for pathway X; and $\Delta\Delta G_X^\ddagger$ is the difference in the barrier heights; and R is the gas constant, T the temperature. Note that the Eyring Equation pre-exponential factor cancels when comparing the ratio of the rate constants. Thus, using the calculated $\Delta\Delta G_X^\ddagger$ value (difference of barrier heights between competing TSs) at the reaction temperature (e.g., 25°C = 298.15K), we are able to obtain the ratio of competing rates.

Fukui reactivity index calculation

To quantify which of the oxygen atoms (oxetane oxygen or acyclic ether oxygen) in substrate **8** is more nucleophilic, we calculated the local Fukui reactivity index at each site. The Fukui index for electrophilic attack (as a nucleophile) at molecular site k is given by⁴¹

$$f_k^- = q_k(N) - q_k(N-1)$$

where $q_k(N)$ is the charge of the neutral system (with N electrons) at site k and $q_k(N-1)$ is the charge of the radical cationic system (with $N-1$ electrons) at site k .

Using the SMD(DMF)-M06-2X/def2-SVP optimized geometry, we computed single point Hirshfeld charges of both the neutral and radical cationic systems of the substrate at the same geometry and obtained the Fukui index for electrophilic attack at oxetane oxygen as 0.322 a.u. and at ether oxygen as 0.006 a.u., showing that the oxetane oxygen is much more nucleophilic (more prone to electrophilic attack) than the ether oxygen.

Optimised structures and absolute energies

Geometries of all optimised structures (in .xyz format with their associated gas-phase energy in Hartrees) are included in a separate folder named *DFT_optimised_structures* with an associated readme.txt file. All these data have been uploaded to zenodo.org (DOI: [10.5281/zenodo.14538630](https://doi.org/10.5281/zenodo.14538630)).

Absolute values (in Hartrees) for SCF energy, zero-point vibrational energy (ZPE), enthalpy and quasi-harmonic Gibbs free energy (at 25°C/298.15 K) for optimized structures are given below. Single point corrections in SMD DMF using M06-2X/BS2 level of theory are also included.

Structure	E/au	ZPE/au	H/au	T.S/au	qh-G/au	SP
substrate	-655.849811	0.288525	-655.54566	0.057971	-655.599971	-656.5926142
bromide	-2574.059928	0	-2574.0576	0.015517	-2574.073085	-2574.363403
Br2CO	-5260.975548	0.00971	-5260.9606	0.032407	-5260.992996	-5261.72158
DMF	-248.216806	0.103124	-248.10669	0.033031	-248.13966	-248.5070715

I	-10581.82101	0.114198	-10581.692	0.057179	-10581.74653	-10583.36853
TS1	-10581.82046	0.113563	-10581.693	0.055025	-10581.74574	-10583.36754
INT1	-10581.82104	0.11363	-10581.693	0.055659	-10581.74653	-10583.36832
TS2	-10581.80571	0.111995	-10581.68	0.054286	-10581.73241	-10583.35336
INT2	-10581.81965	0.112284	-10581.691	0.064122	-10581.74973	-10583.37052
II	-2746.772993	0.101125	-2746.6645	0.035584	-2746.699913	-2747.277628
INT3	-3402.635749	0.391366	-3402.2206	0.079893	-3402.293186	-3403.878769
TS3	-3402.625902	0.391533	-3402.2116	0.077724	-3402.282416	-3403.86446
III	-5976.704955	0.393473	-5976.2864	0.082751	-5976.362044	-5978.246531
TS4	-5976.700197	0.391769	-5976.2835	0.08305	-5976.359241	-5978.241997
IV	-5976.789361	0.39466	-5976.3694	0.08376	-5976.445347	-5978.329091
TS5	-5976.742723	0.391524	-5976.3262	0.08181	-5976.40119	-5978.286705
INT4	-5976.780723	0.391324	-5976.3636	0.083538	-5976.440136	-5978.327927
V	-5728.548621	0.286773	-5728.2436	0.066218	-5728.305158	-5729.809409
INT3b	-11237.67967	0.403851	-11237.244	0.101	-11237.33455	-11239.96411
TS3b	-11237.66762	0.404489	-11237.233	0.096893	-11237.32021	-11239.94996
VI	-11237.66806	0.405202	-11237.232	0.097986	-11237.32029	-11239.94955
TS4b	-11237.66183	0.403707	-11237.228	0.096297	-11237.31485	-11239.94394
INT4b	-11237.73213	0.405147	-11237.297	0.094309	-11237.3826	-11240.01287
INT3a	-3402.63328	0.391475	-3402.218	0.078755	-3402.289811	-3403.876437
TS3a	-3402.614125	0.393729	-3402.1985	0.072125	-3402.265754	-3403.852109
VIII	-5976.687681	0.394564	-5976.2681	0.082211	-5976.343059	-5978.229323
TS4a	-5976.672982	0.392213	-5976.2559	0.0814	-5976.330526	-5978.215335
INT4a	-5976.736987	0.392593	-5976.3182	0.088127	-5976.396784	-5978.282131
TS4a'	-5976.674673	0.392427	-5976.2578	0.078444	-5976.330744	-5978.214821
IX	-2805.437679	0.106926	-2805.3234	0.037042	-2805.359594	-2806.011864
X	-3171.293752	0.284973	-3170.9911	0.063453	-3171.050186	-3172.266406
TS5a	-3171.252926	0.281628	-3170.9536	0.063791	-3171.012773	-3172.228764
INT5a	-3171.297587	0.281546	-3170.9977	0.064667	-3171.057928	-3172.275704

XI	-2923.071955	0.177104	-2922.8842	0.046171	-2922.928233	-2923.762819
-----------	--------------	----------	------------	----------	--------------	--------------

9. References

1. Rintjema, J., Guo, W., Martin, E., Escudero-Adán, E. C. & Kleij, A. W. Highly chemoselective catalytic coupling of substituted oxetanes and carbon dioxide. *Chem. Eur. J.* **21**, 10754–10762 (2015).
2. Dibchak, D. *et al.*, General synthesis of 3-azabicyclo[3.1.1]heptanes and evaluation of their properties as saturated isosteres. *Angew. Chem. Int. Ed.* **62**, e202304246 (2023).
3. Pan, Y. *et al.*, B(C₆F₅)₃-catalyzed deoxygenative reduction of amides to amines with ammonia borane. *Adv. Synth. Catal.* **361**, 2301–2308 (2019).
4. Park, J. W. & Chung, Y. K. Hydrogen-free cobalt–rhodium heterobimetallic nanoparticle-catalyzed reductive amination of aldehydes and ketones with amines and nitroarenes in the presence of carbon monoxide and water. *ACS Catal.* **5**, 4846–4850 (2015).
5. Felding, J., Nielsen, S. F., Larsen, J. C. H. & Babu, B. R. Novel phosphodiesterase inhibitors. International Patent WO2008104175 A2 (2008).
6. Last, S. J., Raboisson, P. J.-M. B., Rombouts, G., Vandyck, K. & Verschueren, W. G. Sulfamoyl-arylamides and the use thereof as medicaments for the treatment of hepatitis b. International Patent WO2014033176 A1 (2014).
7. Gadekar, P. K. *et al.*, Design, synthesis and biological evaluation of novel azaspiro analogs of linezolid as antibacterial and antitubercular agents. *Eur. J. Med. Chem.* **122**, 475–487 (2016).
8. Frisch, M. J. *et al.*, Gaussian 16, Revision B.01. 2016.
9. Zhao, Y. & Truhlar, D. G. The M06 suite of density functionals for main group thermochemistry, thermochemical kinetics, noncovalent interactions, excited states, and transition elements: Two new functionals and systematic testing of four M06-class functionals and 12 other function. *Theor. Chem. Acc.* **120**, 215–241 (2008).
10. Weigend, F. & Ahlrichs, R. Balanced basis sets of split valence, triple zeta valence

- and quadruple zeta valence quality for H to Rn: Design and assessment of accuracy. *Phys. Chem. Chem. Phys.* **7**, 3297–3305 (2005).
11. Hellweg, A. & Rappoport, D. Development of new auxiliary basis functions of the karlsruhe segmented contracted basis sets including diffuse basis functions (Def2-SVPD, Def2-TZVPPD, and Def2-QVPPD) for RI-MP2 and RI-CC calculations. *Phys. Chem. Chem. Phys.* **17**, 1010–1017 (2014).
 12. Weigend, F. Accurate coulomb-fitting basis sets for H to Rn. *Phys. Chem. Chem. Phys.* **8**, 1057–1065 (2006).
 13. Marenich, A. V., Cramer, C. J. & Truhlar, D. G. Universal solvation model based on solute electron density and on a continuum model of the solvent defined by the bulk dielectric constant and atomic surface tensions. *J. Phys. Chem. B* **113**, 6378–6396 (2009).
 14. Davidson, E. R. & Feller, D. Basis set selection for molecular calculations. *Chem. Rev.* **86**, 681–696 (1986).
 15. Lynch, B. J., Zhao, Y. & Truhlar, D. G. Effectiveness of diffuse basis functions for calculating relative energies by density functional theory. *J. Phys. Chem. A* **107**, 1384–1388 (2003).
 16. Papajak, E., Zheng, J., Xu, X., Leverentz, H. R. & Truhlar, D. G. Perspectives on basis sets beautiful: Seasonal plantings of diffuse basis functions. *J. Chem. Theory Comput.* **7**, 3027–3034 (2011).
 17. Zhang, X. & Paton, R. S. Stereoretention in styrene heterodimerisation promoted by one-electron oxidants. *Chem. Sci.* **11**, 9309–9324 (2020).
 18. Yang, X. *et al.*, Carbene-catalyzed activation of remote nitrogen atoms of (benz)imidazole-derived aldimines for enantioselective synthesis of heterocycles. *Angew. Chem. Int. Ed.* **60**, 7906–7912 (2021).
 19. Li, B. *et al.*, Catalyst control over S(IV)-stereogenicity via carbene-derived sulfinyl azolium intermediates. *J. Am. Chem. Soc.* **146**, 25350–25360 (2024).

20. Song, R. *et al.*, Enantioselective modification of sulfonamides and sulfonamide-containing drugs: Via carbene organic catalysis. *Org. Chem. Front.* **8**, 2413–2419 (2021).
21. Lv, Y. *et al.*, Catalytic atroposelective synthesis of axially chiral benzonitriles via chirality control during bond dissociation and CN group formation. *Nat. Commun.* **13**, 36 (2022).
22. Deng, R. *et al.*, Carbene-catalyzed enantioselective sulfonylation of enone aryl aldehydes: A new mode of breslow intermediate oxidation. *J. Am. Chem. Soc.* **144**, 5441–5449 (2022).
23. Lv, W. X. *et al.*, Programmable selective acylation of saccharides mediated by carbene and boronic acid. *Chem* **8**, 1518–1534 (2022).
24. Yang, X. *et al.*, Atroposelective access to 1,3-oxazepine-containing bridged biaryls via carbene-catalyzed desymmetrization of imines. *Angew. Chem. Int. Ed.* **62**, e202211977 (2022).
25. Wei, L. *et al.*, Chiral phosphoric acid catalyzed asymmetric hydrolysis of biaryl oxazepines for the synthesis of axially chiral biaryl amino phenol derivatives. *Angew. Chem. Int. Ed.* **62**, e202306864 (2023).
26. Luo, Z. *et al.*, Ionic hydrogen bond-assisted catalytic construction of nitrogen stereogenic center via formal desymmetrization of remote diols. *Angew. Chem. Int. Ed.* **63**, e202404979 (2024).
27. Liu, D. *et al.*, Photocatalytic direct para-selective C–H amination of benzyl alcohols: Selectivity independent of side substituents. *Angew. Chem. Int. Ed.* **63**, e202407293 (2024).
28. Zhang, X.; Tan, H.; Liu, J.; Li, Z.; Wang, L.; Chen, B. W. J. CHEMSMART: Chemistry Simulation and Modeling Automation Toolkit for High-Efficiency Computational Chemistry Workflows. *arXiv* **2025**, arXiv:2508.20042.
29. Grimme, S. Supramolecular binding thermodynamics by dispersion-corrected

- density functional theory. *Chem.: Eur. J.* **18**, 9955–9964 (2012).
30. Bryantsev, V. S., Diallo, M. S., Goddard III, W. A. & Goddard, W. A. Calculation of solvation free energies of charged solutes using mixed cluster/continuum models. *J. Phys. Chem. B*, **112**, 9709–9719 (2008).
 31. Tan, T.-D.; Serviano, J. M. I.; Luo, X.; Qian, P. C.; Holland, P. L.; Zhang, X.; Koh, M. J. Congested C(Sp³)-Rich Architectures Enabled by Iron-Catalysed Conjunctive Alkylation. *Nat. Catal.* **2024**, 7 (3), 321–329.
 32. Tan, T.-D.; Tee, K. Z.; Luo, X.; Qian, P. C.; Zhang, X.; Koh, M. J. Kinetically Controlled Z-Alkene Synthesis Using Iron-Catalysed Allene Dialkylation. *Nat. Synth.* **2025**, 4 (1), 116–123.
 33. Contreras-García, J. *et al.*, NCIPLOT: A program for plotting noncovalent interaction regions. *J. Chem. Theory Comput.* **7**, 625–632 (2011).
 34. Schrödinger, L. *The PyMOL Molecular Graphics Development Component, Version 1.8*; 2015.
 35. Grimme, S. Exploration of chemical compound, conformer, and reaction space with meta-dynamics simulations based on tight-binding quantum chemical calculations. *J. Chem. Theory Comput.* **15**, 2847–2862 (2019).
 36. Pracht, P., Bohle, F. & Grimme, S. Automated exploration of the low-energy chemical space with fast quantum chemical methods. *Phys. Chem. Chem. Phys.* **22**, 7169–7192 (2020).
 37. Bannwarth, C., Ehlert, S. & Grimme, S. GFN2-XTB - an accurate and broadly parametrized self-consistent tight-binding quantum chemical method with multipole electrostatics and density-dependent dispersion contributions. *J. Chem. Theory Comput.* **15**, 1652–1671 (2019).
 38. Grimme, S., Bannwarth, C. & Shushkov, P. A robust and accurate tight-binding quantum chemical method for structures, vibrational frequencies, and noncovalent interactions of large molecular systems parametrized for all spd-block elements (Z

- = 1-86). *J. Chem. Theory Comput.* **13**, 1989–2009 (2017).
39. Bannwarth, C. *et al.*, Extended tight-binding quantum chemistry methods. *Wiley Interdiscip. Rev. Comput. Mol. Sci.* **11**, e1493 (2021).
40. Hirshfeld, F. L. Bonded-atom fragments for describing molecular charge densities. *Theor. Chim. Acta* **44**, 129–138 (1977).
41. Yang, W. & Mortier, W. J. The use of global and local molecular parameters for the analysis of the gas-phase basicity of amines. *J. Am. Chem. Soc.* **108**, 5708–5711 (1986).